Aerosols and Clouds data processing and optical properties retrieval algorithms for the spaceborne ACDL/DQ-1

Guangyao Dai[1], Songhua Wu[1,2,3], Wenrui Long[1], Jiqiao Liu[4], Yuan Xie[4], Kangwen Sun[1], Fanqian Meng[1], Xiaoquan Song[1,2], Zhongwei Huang[5], Weibiao Chen[4]

5 [1]College of Marine Technology, Faculty of Information Science and Engineering, Ocean University of China, Qingdao, 266100, China
[2]Laoshan Laboratory, Qingdao, 266200, China
[3]Institute for Advanced Ocean Study, Ocean University of China, Qingdao, 266100, China
[4]Key Laboratory of Space Laser Communication and Detection Technology, Shanghai Institute of Optics and Fine Mechanics,
10 Chinese Academy of Sciences, Shanghai 201800, China
[5]Key Laboratory for Semi-Arid Climate Change of the Ministry of Education, College of Atmospheric Sciences, Lanzhou University, Lanzhou, 730000, China

Correspondence to: Songhua Wu (wush@ouc.edu.cn)

Abstract. The new-generation atmospheric environment monitoring satellite DQ-1, launched successfully in April 2022
15 carries the Aerosol and Carbon Detection Lidar (ACDL) which is capable of globally profiling the aerosols and clouds optical properties with high accuracy. The ACDL/DQ-1 is a high-spectral-resolution lidar (HSRL) with two-wavelength polarization detection, that can be utilized to derive the aerosol optical properties. The methods are specifically developed for the data processing and optical properties retrieval according to the specific characteristics of the ACDL system are introduced in detail in this paper. Considering the different signal characteristics and different background noise behaviours of each channel during
20 daytime and nighttime, the procedures of data pre-processing, denoising process and quality control are applied to the original measurement signals. The aerosol and cloud optical properties products of the ACDL/DQ-1 including total depolarization ratio, backscatter coefficient, extinction coefficient, lidar ratio and colour ratio can be calculated by the retrieval algorithms presented in this paper. Two measurement cases with use of the ACDL/DQ-1 on 27th June 2022 and the global averaged aerosol optical depth (AOD) from 1st June to 4th August 2022 are provided and analysed, which demonstrated the measurement capability of
25 the ACDL/DQ-1.

1 Introduction

Aerosols and clouds greatly affect the Earth's climate through their direct and indirect impact on the radiation budget. The altitude of the cloud layers and their multi-layer structures can influence the radiative balance of the earth–atmosphere system by reflecting sunlight and absorbing thermal radiation. The aerosol radiation forcing significantly affects the atmospheric
30 physical and chemical processes (Boucher et al. 2013). Therefore, as one of the largest uncertainties in global climate model, aerosols and clouds bring inaccuracy in estimating the climate change and weather forecasting (IPCC 2014). Several studies show that local aerosols events also affect global climate change on a larger scale (IPCC 2021; Dai et al. 2022). The satellite-

based observations have great potential to acquire the global aerosols and clouds information. As a well-developed active sensing tool, lidars could provide aerosols and clouds profile measurements with high accuracy and high spatiotemporal

35 resolution (King et al. 1999; Winker et al. 2007). The Cloud-Aerosol Lidar and Infrared Pathfinder Satellite Observation (CALIPSO) satellite was launched in April 2006, with a primary payload of Cloud-Aerosol Lidar with Orthogonal Polarization (CALIOP) (Hunt et al. 2009). CALIOP produces a dataset of global vertically resolved cloud and aerosol properties which gives inspiring insights to understanding the role of aerosols and clouds in the climate system (Winker et al. 2009). However, it is difficult to measure the lidar radio with CALIOP due to that the Mie scattering and Rayleigh scattering are mixed in the

40 echo signal (Sayer et al. 2012). CALIOP has developed a Hybrid Extinction Retrieval Algorithm (HERA) which retrieves particulate backscatter and extinction profiles from attenuated backscatter profile by combining the scene classification (Young et al. 2009). By improving the algorithms for aerosol classification and lidar ratio selection, the accuracy of the inversion can be improved to some extent (Young et al. 2018). The previous studies have shown that a relatively large uncertainty would appear in extinction coefficient retrievals of aerosols and clouds as the lidar ratio is selected or modelled (Schuster et al. 2012;

45 Balmes et al. 2019).

Taking advantage of the different spectral broadening, high-spectral-resolution lidar (HSRL) can separate the aerosol contribution from the molecular backscatter with a narrow bandwidth optical filter. Thus, without assuming the lidar ratio, the aerosol backscatter and extinction coefficients could be obtained respectively. Many HSRL instruments have been successfully implemented to measure the atmospheric parameters or particle optical properties by means of ground-based lidars and

50 airborne lidars (Esselborn et al. 2008; Li et al. 2008; Müller et al. 2014). The Aeolus, which carries a Fabry-Pérot interferometer based wind lidar, was successfully launched in 2018. It could provide the atmospheric optical properties by independently measure the particle extinction coefficients, co-polarized particle backscatter coefficients and the co-polarized lidar ratio by the standard correct algorithm (SCA) (Flament et al. 2008; Flament et al. 2021). And Aeolus optimizes aerosol optical properties by maximum likelihood estimation, due to the noise sensitivity of the SCA as an algebraic inversion scheme (Ehlers

55 et al. 2022). The Earth Clouds, Aerosols and Radiation Explorer (EarthCARE), which deploys a HSRL Atmospheric Lidar (ATLID) (Illingworth et al. 2015), is scheduled to be launched in 2024.

The Chinese first atmospheric environment monitoring satellite DQ-1 has been successfully launched on 16th April 2022. As an integrated detection scientific research satellite, it will serve as an important part of Chinese atmospheric environment monitoring system. The DQ-1 is operated in a sun-synchronous orbit at the altitude of 705 km and provides global

60 comprehensive monitoring of atmospheric particles, carbon dioxide (CO_2), aerosols and clouds. For the combination of the active and passive measurements, the DQ-1 equips five sensors including an Aerosol and Carbon Detection Lidar (ACDL), a Particulate Observing Scanning Polarimeter (POSP), a Directional Polarization Camera (DPC), an Environmental trace gas Monitoring Instrument (EMI) and a Wide Swath Imaging system (WSI). The primary payload carried by the DQ-1 is the ACDL, which is a lidar system consisting of two different modules. One is the aerosol-measurement module which provides

65 aerosols and clouds profile measurements with high accuracy globally, and another is the CO_2-measurement module for atmospheric column CO_2 observations (Chen et al., 2023). In previous studies, the ACDL scientific team measured the

transmittance of the different absorption lines under different temperatures of the iodine wall and finger (Dong et al. 2018). The reliability of the space-borne system was confirmed through simulation and performance evaluation (Liu et al. 2019; Yu et al. 2018), and the impact of errors was also assessed (Zhang et al. 2018). Finally, the algorithmic and theoretical foundation

70 for the spaceborne HSRL loaded on DQ-1 is established. The airborne ACDL prototype (A2P) was developed and mounted on an airplane to conduct the calibration and validation experiments over Qinhuangdao, China, in March 2019. The spatial and temporal developments of the atmospheric boundary layer (ABL) and aerosol distribution along the flight routes were obtained in this experiment (Wang et al. 2020; Ke et al. 2022).

In this paper, the ACDL Aerosol module (ACDL-A) measurement principles are introduced. The retrieval methods applied

75 for the aerosol optical properties calculation are presented. Finally, two long-term global aerosol optical properties distribution measurement cases are provided. In this work, a data pre-processing process is designed that fits the characteristics of ACDL laser transmitting, receiving and data acquisition. The data quality control and segmentation denoising algorithms used in data processing show considerable noise suppression capabilities.

The paper is organized as follows. Section 2 describes the composition and working principle of the ACDL-A. Section 3 and

80 section 4 contain the detailed description of the data processing and the optical properties retrieval algorithms. In section 5 we provide two measurement cases of optical parameter products and two months of global observations in order to demonstrate the capabilities of the presented algorithms. Conclusions and prospects are summarized in section 6.

2. Overview of the ACDL-A

The ACDL consists of a transmitter for generating the laser pulse down through the atmosphere, a receiver for collecting the

85 backscatter lights from the atmospheric particles, a detection and data acquisition that measures signal strength and prepares for data downlink. The functional description of ACDL is provided in Fig 1. The transmitter contains a three-wavelength laser which emits laser beams at the wavelengths of 532 nm, 1064 nm and 1572 nm. The output pulse energies at each wavelength are monitored by the energy meters. With the repetition frequency of 20 Hz, the laser emits two pulses successively with a time interval of 200 µs. This configuration of the laser emission strategy, which called dual-pulse, has a horizontal resolution

90 of 337 m on the surface for the original profile. Because of the design of dual-pulse, we present a practical data process which is described in detail in section 3.
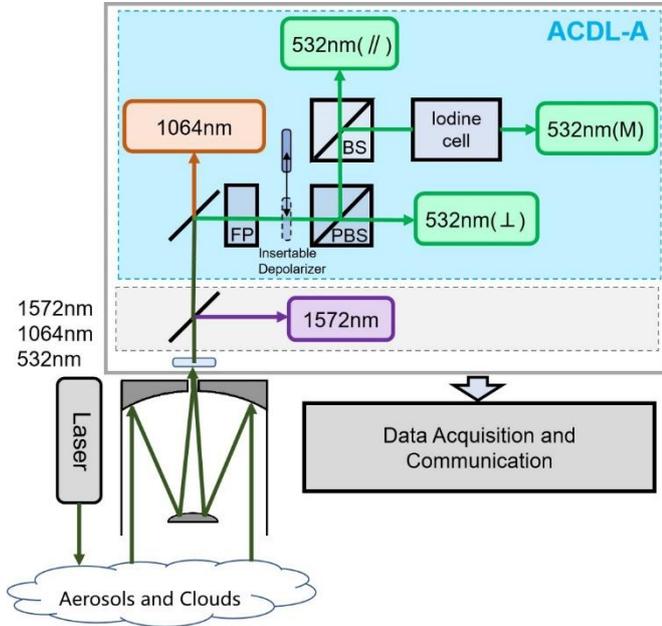
Figure 1: Schematic diagram of ACDL-A.

The ACDL employs an iodine vapor absorption filter to block the Mie scattering, while to transmit the Rayleigh scattering
light. As shown in Fig. 1, the backscatter lights are divided into 532 nm channels (including cross-polarized and parallel-polarized channels and high-spectral-resolution channel) and 1064 nm channel in the spectroscopic module. The cross-polarized and parallel-polarized channels at 532 nm are designed for the measurements of the linear particle depolarization
ratio. After reflected by the polarization beam splitter (PBS), the lights are split again by a beam splitter (BS) and a portion of
the parallel-polarized signal passes through the iodine absorption filter, thus constituting the molecular channel to estimate the
optical properties of aerosol particles and clouds. Additionally, the 1064 nm channel adopts the same sampling frequency as
532 nm channels for atmospheric detection in the ACDL-A.

To facilitate the distinction of the parameters of each channel, the 1064 nm channel is denoted with subscript "1064", while
the 532 nm channels are not specifically marked with the wavelength subscript. The superscripts of $\parallel$, $\perp$, and M are used to
represent the parallel-polarized channel, cross-polarized channel and high-spectral-resolution channel at 532 nm, respectively.

The signal intensity of these four channels in ACDL-A module can be expressed using the lidar equations as follows:

$$P^{\parallel}(z,\lambda) = E \frac{c^{\parallel} K^{\parallel}}{(z-z_0)^2} [\beta_m^{\parallel}(z,\lambda) + \beta_a^{\parallel}(z,\lambda)] T^2(z,\lambda) \, , \tag{1}$$

$$P^{\perp}(z,\lambda) = E \frac{c^{\perp} K^{\perp}}{(z-z_0)^2} [\beta_m^{\perp}(z,\lambda) + \beta_a^{\perp}(z,\lambda)] T^2(z,\lambda) \, , \tag{2}$$

$$P^{M}(z,\lambda) = E \frac{c^{M} K^{M}}{(z-z_0)^2} [f_m \beta_m^{M}(z,\lambda) + f_a \beta_a^{M}(z,\lambda)] T^2(z,\lambda) \ \text{and} \tag{3}$$

$$P(z, \lambda_{1064}) = E_{1064} \frac{C_{1064}K_{1064}}{(z-z_0)^2}[\beta_m(z, \lambda_{1064}) + \beta_a(z, \lambda_{1064})]T^2(z, \lambda_{1064}) , \tag{4}$$

110 where $P(z, \lambda)$ is the measured power at the height of z received by the channel with the wavelength of λ, and E is the single pulse energy, C and K represent the calibration constants and the system constants containing optical efficiency and gain coefficients. $(z - z_0)$ is the distance between the altitude where the detected particle is located and the satellite altitude. β denotes the backscatter coefficient at z with a certain wavelength and uses the subscripts m and a represent the molecule and particle (aerosols and clouds). And T^2 is the round-trip transmittance between observation area z and z_0. The transmittance of

115 iodine filter for aerosol scattering and molecular scattering are denoted by f_a and f_m, which are function of height due to its dependence on atmospheric temperature and pressure.

The molecular backscattering coefficient β_m and the molecular extinction coefficient α_m can be calculated according to the Rayleigh scattering theory (Bodhaine et al. 1999; Collis and Russell 1976), and the inversion of the aerosol optical parameters can be achieved by combining the above equations.

120 **3. ACDL-A data preparation**

As shown in Fig. 2, the ACDL-A data processing procedure consists of data preparation, pre-processing and optical properties retrieval. This section describes the data preparation of removing the background noise from the original voltage signal returned through the sub-channel and correcting its elevation. Additionally, the auxiliary data prepared for the inversion algorithm are also introduced in this section.
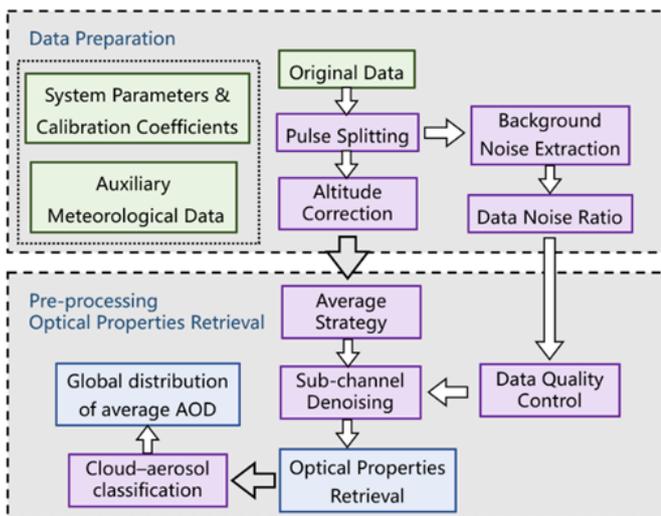
125

Figure 2: Flowchart of the ACDL-A data process. The green box represents the input data, the purple box shows the data processing step, and the blue part indicates the output data products.

3.1 Dual-pulse data processing

The laser in the ACDL-A transmitter applies a unique dual-pulse emission configuration, which emits a pair of pulses
130   continuously with a repetition frequency of 20 Hz. In other words, the laser emits a total of 40 pulses in one second, where
every pair of pulses are grouped together and the first pulse (odd-pulse) is launched 200 μs before the second pulse (even-
pulse). As shown in Fig. 3, after triggering a set of dual-pulse, the blue line at 16.1 μs is the duration of odd-pulse emission
and the orange line is the even-pulse emission duration. The time between the emission of odd-pulse (the blue line) and the
start of signal acquisition (the blue dashed line) is referred to as "TimeDelay". After completing the full height data acquisition
135   of the odd-pulse, the backscatter signals stimulated by the even-pulse are acquired immediately afterwards. Since all the
channels of ACDL-A are sampled with a frequency of 50 MHz in the data acquisition module, the corresponding fundamental
vertical spatial resolution is 3 m. To improve the satellite data downlink transfer efficiency, as shown in Fig. 3, the original
data is 8-bin averaged at high altitude.
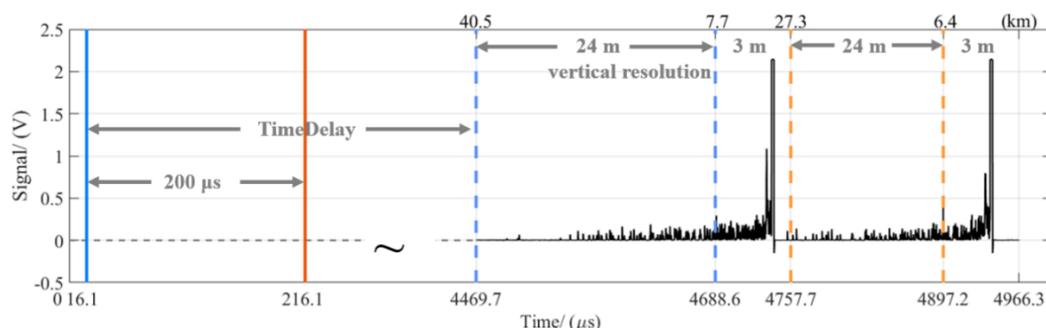
140   **Figure 3: Timing diagram for dual-pulse emission and acquisition.**

Since the original signal contains two pulses with different height resolution data, it is necessary to match odd-pulse and even-
pulse in altitude separately in the data preparation phase. The latitude and longitude of the laser footprint points corresponding
to each set of dual-pulse were determined using spacecraft attitude and ephemeris data. Based on the time of launch and
acquisition, the position of each data point relative to the satellite can be calculated. The ellipsoidal heights corresponding to
145   each data point of the odd-pulse and even-pulse are calculated separately by the WGS-84 (Lohmar 1988) coordinate system,
which enables the separation of the dual-pulse.

3.2 Sub-channel background denoising

In previous studies, the background noise was usually removed by subtracting the mean values of the "signals" at high-altitude
during the data processing of satellite-based Lidars (Luthcke et al. 2021; Kar et al. 2018). The high-altitude "signals" are
150   selected because that only the background noise due to the solar and dark-counts from detectors are included in the "signals".
Due to the special data acquisition strategy of the dual-pulse configuration, the maximum observation altitude of the odd-pulse
could be higher than 40 km (maximum detection altitude is jointed determined by the latitude and elevation). As shown in Fig.
3, after completing the signal acquisition of odd-pulse, the maximum observation altitude collected for the even-pulse is about

27 km. Hence the signal of odd-pulse is selected for background noise extraction in each channel. To avoid the effect of
155 possible aerosol layers at high-altitude, the minimum value of the segmented-averaged signal in parallel-polarized channel and
cross-polarized channel of 532 nm are selected as background noise, while the signals at high altitude are removed as
background noise in high-spectral-resolution channel and 1064 nm channel.

The amplitude of background noise in each channel is closely related to the observed location and time period. Figure 4 (a1)
to (a4) and Figure 4 (b1) to (b4) show the background noises extracted from each channel during nighttime and daytime,
160 respectively. The background noise of the 532 nm parallel-polarization channel is relatively stable and varies from 0.002 V to
0.005 V during nighttime. During daytime, due to the different irradiance at different locations and underlying surfaces, the
background noise fluctuates at the range of 0.002 V to 0.5 V. The background noises of cross-polarized channel and high-
spectral-resolution channel manifest similar characteristics. The cross-polarized channel background noise level at nighttime
is more stable at around 0.005 V while it is more sensitive and even reaches to 1.5 V at daytime. The high-spectral-resolution
165 channel background noise is normally below 0.002 V at nighttime and is increased obviously during the daytime. The aerosol
backscatter signal from the 1064 nm channel is slightly affected by sunlight. The high values of the initial sets of nighttime
observations in Fig. 4 (a1) to (a3) may result from the remaining solar radiation at dusk.
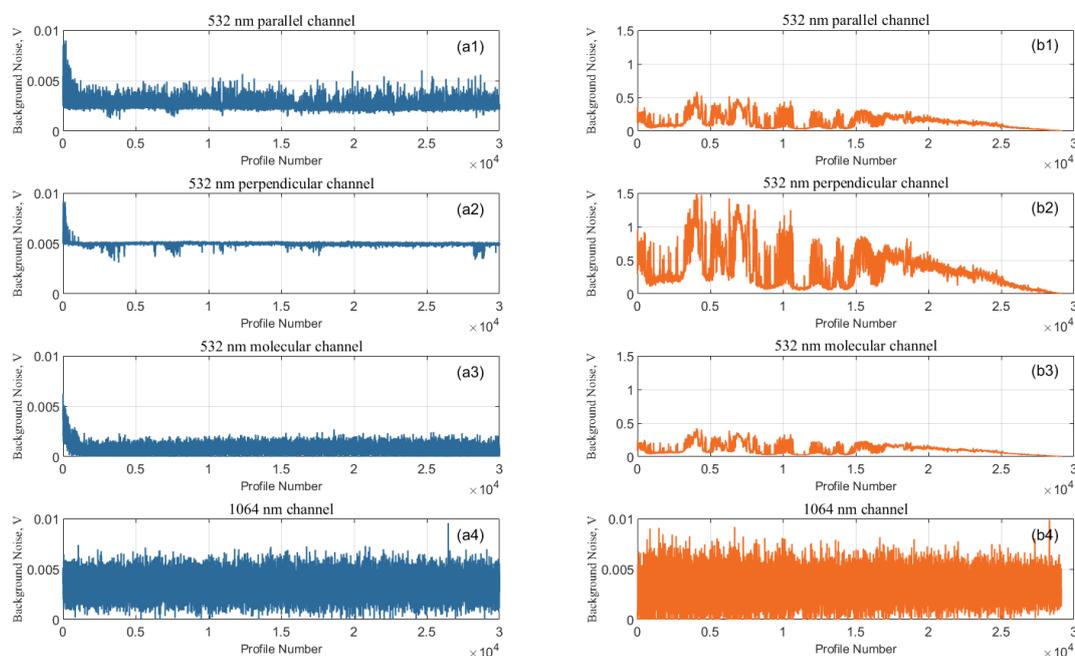
Figure 4: The background noise value subtracted from each echo signal in nighttime (blue dash on the left) or daytime (orange dash
170 **on the right) segment of data, both on June 27, 2022. Corresponding to each channel in order from top to bottom, (a1, b1) parallel-**
polarized channel at 532 nm, (a2, b2) cross-polarized channel at 532 nm, (a3, b3) molecular channel at 532 nm, and (a4, b4) 1064
nm channel.

3.3 Auxiliary datasets preparation

The auxiliary datasets contain the system parameters and meteorological data. The system parameters C and K for each
175 channel are provided by the ACDL scientific team which will be not discussed in this paper. The main meteorological datasets required in the inversion algorithms include the atmospheric temperature and pressure. The calculation of the transmittance of iodine filter for molecular scattering f_m is highly reliant on them. The global temperature, ozone mass mixing ratio and pressure data are collected from the European Centre for Medium-range Weather Forecasts (ECMWF) fifth-generation reanalysis (ERA5) dataset (Hersbach et al., 2020). The ERA5 data provides hourly averaged global atmospheric parameters
180 with a 0.25° latitude × 0.25° longitude resolution grid with 37 pressure levels. The ERA5 global data are matched according to the latitude and longitude of the ACDL-A, and the pressure gradient data is then matched to the corresponding altitude of the lidar signal using the cubic spline interpolation.

4. Retrieval algorithms

4.1 Pre-processing

185 **4.1.1 Average strategy and quality control**

To improve the signal quality and reduce the interference of transient clutter, the raw data of each channel are averaged vertically and horizontally. After the assessments of different averaging scales, the vertical averaging scale of 50 m and horizontal averaging scale of 3.3 km (10 pairs of dual-pulses) for nighttime data are chosen in this work. Considering that the solar background radiation at daytime brings lower signal-to-noise ratio and more noise clutter, a wider range of averaging
190 scale is applied during daytime. The daytime measurement data from high-spectral-resolution channel are averaged with the vertical scale of 50 m and horizontal scale of 10 km (30 pairs of dual-pulses). As shown in Fig. 5, with the averaging strategy presented above, the optical power signals at each channel during different scenarios are calculated with considering the systematic parameters.
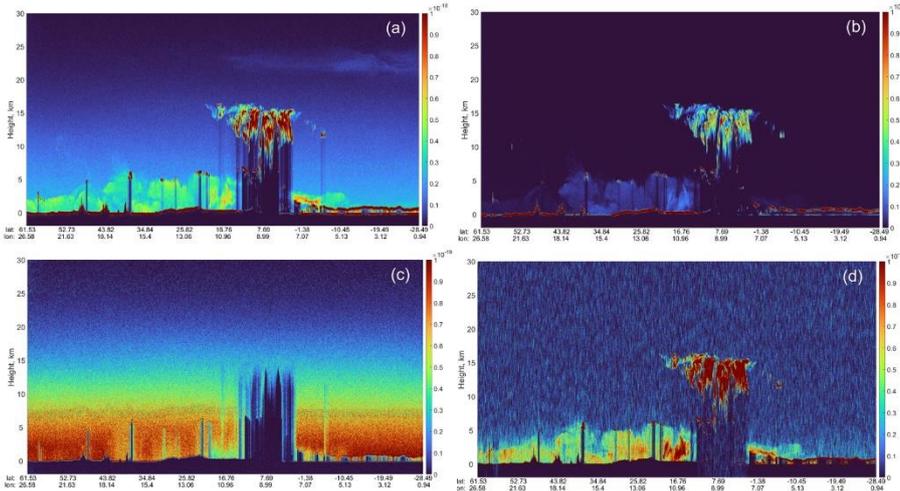
Figure 5: ACDL-A optical power signals in (a) 532 nm parallel polarized channel, (b) 532 nm perpendicular polarized channel, (c) 532 nm molecular channel and (d) 1064 nm channel on 00:45:23 UTC to 01:10:22 UTC on June 27, 2022.

From Fig. 5, the cloud layers at about 6-16 km and aerosol layers within the atmospheric boundary layer are observed in the parallel-polarized channel and cross-polarized channel after pre-processing procedure. However, the high-altitude aerosol layer at about 25 km is only captured by the parallel-polarized channel with a faint signal, showing weak depolarization characteristics. With more disorderly noises and larger fluctuations of signal noise, the signal intensity from high-spectral-resolution channel is one order of magnitude weaker than the other channels. Hence it is more crucial to denoise the high-spectral-resolution channel signals in the subsequent retrieval algorithms. The 1064 nm band almost has no response to molecular backscattering, and its optical power signal with low aerosols and clouds content behaves as a weakly fluctuating noise.

To evaluate the single channel echo signal quality, a parameter named Data-to-Noise Ratio (DNR) is introduced to calculate the ratio of the signal and subtracted background noise P_{noise} at a certain height. The DNR is calculated by Equation (5):

$$DNR(z,\lambda) = \frac{P(z,\lambda)+P_{noise}}{P_{noise}} . \qquad (5)$$

The DNR can be used for the data quality control by setting reasonable thresholds for daytime-nighttime scenarios for each channel. It will serve as the segmentation basis for the high-spectral-resolution channel denoising algorithm in the following subsection.

4.1.2 Sub-channel denoising algorithm

As discussed in the previous sections, the noise of the power signal of each channel remains. Due to the different optical path designs of channels in the ACDL, the signal characteristics behave distinctly. In this work, a set of sub-channels denoising algorithms is designed especially for each channel as shown in Fig. 6. The target of the denoising algorithm is to reserve the

215 useful information as much as possible from the optical signal data, to remove the high frequency noise and outliers, and to obtain smoother data profiles.
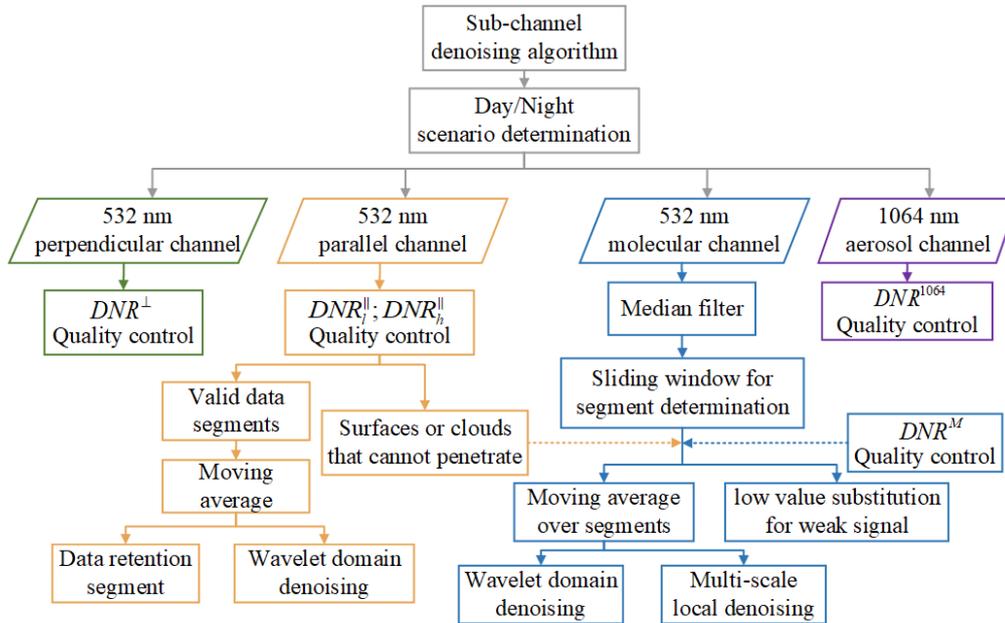
Figure 6: Flowchart of the ACDL-A sub-channel denoising algorithms.

After the data averaging procedure, different thresholds would be chosen for each channel based on the day-night flag in the

220 auxiliary data segment of ACDL-A. Distinct aerosol and cloud layers can be observed in the 532 nm cross-polarized channel and 1064 nm channel echo signals. The desired signal can be extracted from the overall echo profiles using a suitable threshold in the corresponding $DNR^\perp$ and DNR^{1064} profiles. The parallel-polarized channel signal is divided into three parts using $DNR^\parallel$ thresholds. At low altitudes, the data quality is high and the valid data segment contains aerosols echo information which needs to retain as much of the original signal variations as possible. At high altitudes, the noise is removed using wavelet

225 bases technique. The detailed process is presented in Fig. 6. The echo signal is rapidly saturated at thick clouds that cannot be penetrated or at Earth's surface, and that height position (such as the purple dashed line in Fig. 7) is localized in the corresponding high-spectral-resolution channel signal. To make the observed profiles have better spatial continuity, the denoising of the high-spectral-resolution channel is first performed with a 2-D median filter, and then a sliding window is used to denoise the segments of each profile, with the overall goal of obtaining a smoother profile that can represent the trend of the

230 signal.
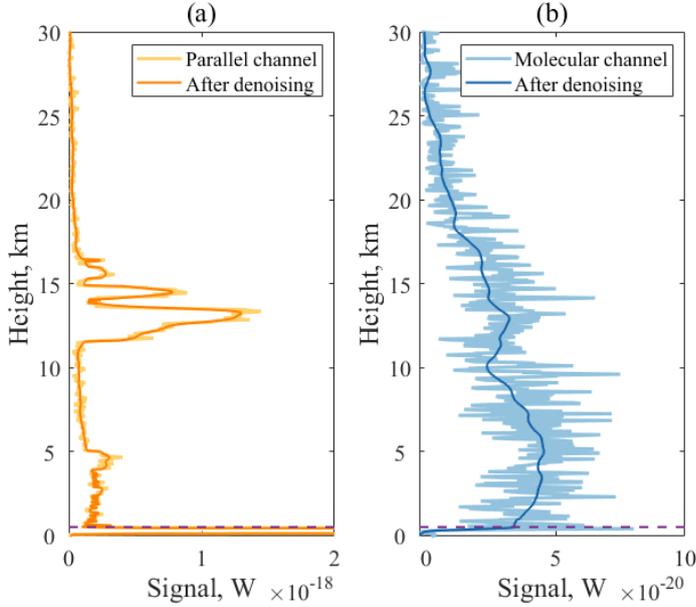
Figure 7: 532 nm parallel polarized channel (a) and molecular channel (b) denoised profiles, the light color line is the original signal, the dark color line is after denoising.

The signals of each channel after segmentation and denoising are re-spliced according to the height in a way that maintains

235   local continuity. After the data pre-processing has been completed, the *DNR* is still used in subsequent inversion algorithms

to represent the quality of the data.

4.1.3 Optical Properties Retrieval

The aerosols and clouds optical properties products of ACDL/DQ-1 include total depolarization ratio, backscatter coefficient,

extinction coefficient, lidar ratio and color ratio.

240   The total depolarization ratio $\delta(z)$ is the ratio of total backscattering coefficient in the vertical polarization direction to that in

the parallel polarization direction, which is used to describe the shape characteristics of the aerosol particles and is related to

the degree of regularity of the particle shape. The total depolarization ratio can be calculated via:

$$\delta(z) = \frac{\beta_m^{\perp}(z) + \beta_a^{\perp}(z)}{\beta_m^{\parallel}(z) + \beta_a^{\parallel}(z)} = \frac{P^{\perp}(z,\lambda)C^{\parallel}K^{\parallel}}{P^{\parallel}(z,\lambda)C^{\perp}K^{\perp}} \,. \tag{6}$$

With the high-spectral-resolution channel, the ACDL-A enables direct detection of aerosol backscattering coefficient $\beta_a(z)$

245   and extinction coefficient $\alpha_a(z)$ by associating equations (1-3), which are expressed as:

$$\beta_a(z) = \beta_m(z)\frac{[1+\delta(z)][f_m(z)-f_a]\mathcal{R}(z)}{(1+\delta_m)[1-f_a\mathcal{R}(z)]} - \beta_m(z) \;\; \text{and} \tag{7}$$

$$\alpha_a(z) = \frac{\partial \tau(z)}{\partial z} - \alpha_m(z) \,. \tag{8}$$

The temperature and pressure profiles modelled with ERA5 are used to obtain the molecular scattering spectra at each height through the atmospheric model (Tenti et al. 1974), and to calculate the $f_m(z)$ and $\alpha_m(z)$. The δ_m represents the molecular depolarization ratio, which can be also affected by the interference filter specifications and is usually set as a constant. The $\mathcal{R}(z)$ is the backscattering ratio of 532 nm parallel channel signal to the high-spectral-resolution channel signal.

The atmospheric aerosol optical depth (AOD) is defined as the integral of the aerosol extinction coefficient and molecular extinction coefficient over all heights. Conversely the gradient of AOD over height can be used to calculate α_a. And the $\tau(z)$ can be calculated from the transmittance as in Equation (9):

$$\tau(z) = -\frac{1}{2} ln[T^2(z,\lambda)] . \tag{9}$$

The multiple scattering of clouds is considered in this algorithm, where division by the multiple scattering factor η represents the required correction of the measured transmittance (Hu 2007; Garnier et al. 2015).

The magnitude of aerosol lidar ratio $S_a(z)$ is influenced by the aerosol absorption and scattering characteristics and is one important parameter to distinguish the aerosol types. As shown in Equation (10), it is calculated as the ratio of the aerosol extinction coefficient to the backscattering coefficient:

$$S_a(z) = \frac{\alpha_a(z)}{\beta_a(z)} . \tag{10}$$

The ACDL-A has a dual-wavelength observation capability of obtaining the attenuated color ratio $\chi'(z)$, which is defined as the ratio of the attenuated backscatter coefficient $B_\lambda(z)$ at 1064 nm to that at 532 nm, where $B_\lambda(z)$ has been calibrated by the ozone and molecular two-transmittance through the atmosphere (Vaughan et al. 2019):

$$\chi'(z) = \frac{B_{1064}(z)}{B_{532}(z)} . \tag{1}$$

In this algorithm, the gradient calculation on AOD profiles amplifies the noise effect from high-spectral-resolution channel. Although the sub-channel denoising algorithm has been deployed to remove the noises, the uncertainties in the low-quality signal remain.

5. Results and discussion

The size of each segment is limited when ACDL-A data is transmitted back through the satellite transceiver system, and each track data is divided into two views by day and night, and each view contains two segments for subsequent data processing. The following Fig. 8 presents the aerosol optical properties of two segments of ACDL observations at mid-low latitudes on 27th June, 2022.
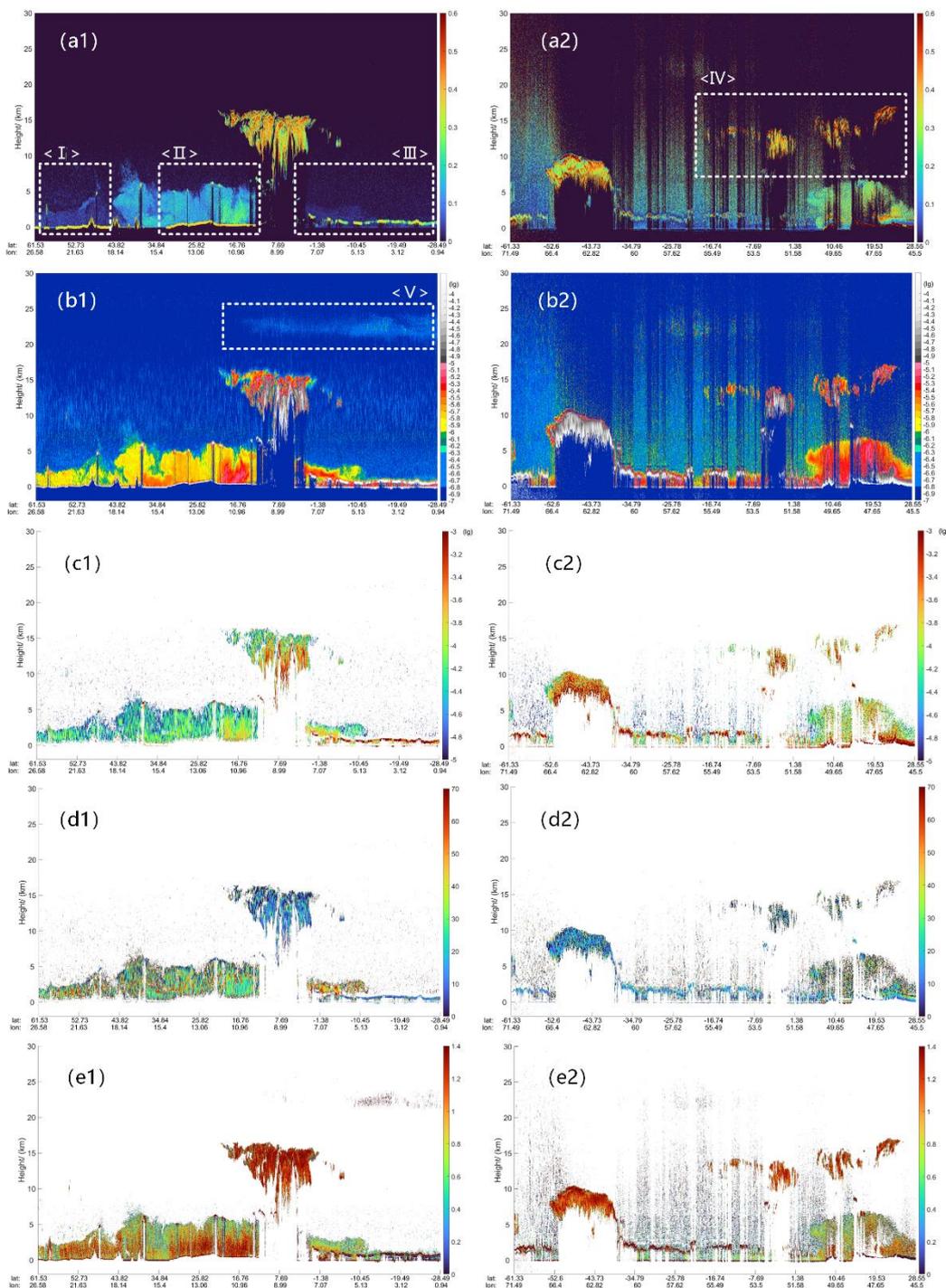
Figure 8: Retrievals from ACDL-A measurements between 00:45:23 and 01:10:22 (nighttime, a1 to e1) and between 09:49:05 and 10:14:05 (daytime, a2 to e2) on June 27, 2022. From top to bottom: The time series of (a1, a2) total depolarization ratio, (b1, b2) aerosol backscattering coefficient, (c1, c2) aerosol extinction coefficient, (d1, d2) aerosol lidar ratio and (e1, e2) attenuated color ratio.

Figure 8 (a1) to (e1) present the retrieval results with high data quality during nighttime. In the Eastern European urban
280   agglomeration (area <I>), the total depolarization ratios are 0.08±0.02 and lidar ratios at 532 nm are 50±20 sr. Thus, it indicates
that the urban pollution aerosols may dominate within the boundary layer in this area (Burton et al. 2012). The satellite flied
over the Sahara Desert with the footprints cross area <II>. The dominant aerosol type changes from urban pollution aerosols
to mixed dust with total depolarization ratio of 0.32±0.03, aerosol lidar ratio of 39±12 sr, and higher extinction coefficient than
that within area <I>. In area <III>, some low-altitude clouds that existed at the range of 6 km and 16 km can be observed over
285   the Atlantic Ocean in the Southern Hemisphere. There are structural features of the aerosol layers in the vertical and horizontal
directions as seen in the optical properties of each area, which are often assumed to be a single type aerosol with the same
optical characteristics in the absence of HSRL.

The daytime observations of aerosols and clouds by ACDL are influenced by the solar light thus behave lower quality
compared to the measurement data during nighttime, as shown in Fig. 8 (a2) to (e2), which are from a segment of data that
290   crosses from the Indian Ocean to the Arabian Peninsula. The superposition of sunlight makes the echo signals of each channel
have larger values, and it is easier to reach signal saturation during daytime. As shown in area <IV>, where the aerosol layers
below the clouds cannot be distinguished from the noise. As shown in area <V> of Fig. 8 (b1), a thin aerosol layer exists at
altitudes of 22-26 km, mainly confined between 15°N and 28°S. This layer of aerosols is likely to be smoke or sulfate from
the January 2022 Tonga eruption (Legras et al. 2022). Due to the low signal strength of this layer, observations are only
295   available in the 532 nm aerosol backscatter coefficient with the current version algorithm.

The data processing and retrieval algorithm consider the reusability of different global observation scenarios and is capable of
processing the ACDL-A data in batches. The data production processing rate can meet the satellite data processing needs after
proper optimization. As shown in Fig. 9 (a), the total column AOD (Pan et al. 2022) is calculated with the aerosol optical
parameters retrieved from ACDL-A data from 1st June to 4th August, 2022. The aerosol profile data are quality screened,
300   removed most clouds by setting thresholds for the optical properties and then aggregated onto a global 0.25°×0.25° latitude-
longitude grid. The global AOD describes the attenuation of light by aerosols and is an important indicator reflecting the degree
of air pollution (Levy et al. 2013), The AOD at different heights could also be obtained with ACDL-A. In Fig. 9 (b), the slice
diagrams show the global distribution of the average AOD in the three height ranges of surface-1 km, 1-3 km, and 3-5 km,
respectively.
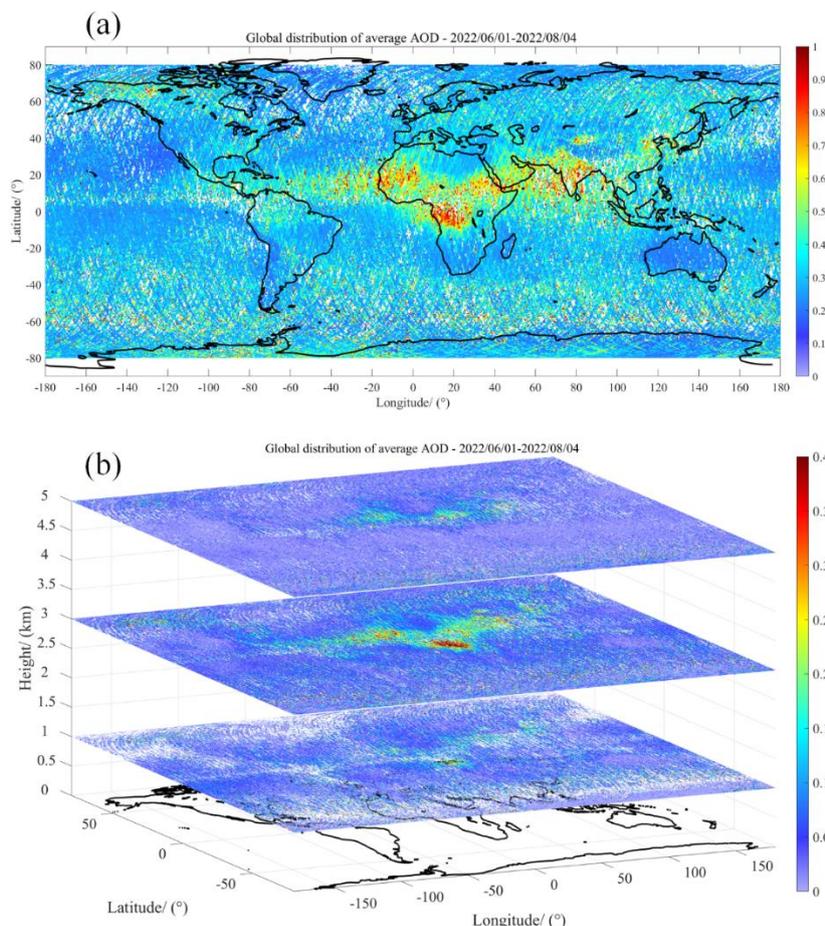
Figure 9: (a) Global whole-layer averaged AOD for June 1, 2022 to August 4, 2022. (b) Slices of the global distribution of AOD at different height range from June 1, 2022 to August 4, 2022.

6. Summary and outlook

This paper gives an overview of the main algorithms applied to derive the aerosols and clouds optical properties product of ACDL/DQ-1. ACDL brings a major advance in spaceborne active remote sensing of aerosols and clouds. The ACDL-A data processing algorithms have unique aspects designed to take advantage of these new capabilities. The ACDL-A data processing procedure consists of data preparation, pre-processing and optical properties retrieval. Based on the unique dual-pulse emission configuration and averaging strategy, the algorithm can deliver data products with the horizontal resolution of 3.3 km and vertical resolution of 50 m. And the developed data pre-processing algorithm considers the effect of solar background light on the data quality of day and night scenes. In view of the data characteristics of different channels, a set of sub-channels denoising algorithms are designed specifically for each channel. The capacity of the ACDL-A to independently measure backscatter coefficient and extinction coefficient is also demonstrated by two observation cases on 27th June 2022, where the retrieved

lidar ratio is calculated as well. The data processing and retrieval algorithms are applied to the long-term ACDL/DQ-1

observation campaign and a measurement case of the average AOD global distribution is provided.

320 The ACDL scientific team is gradually accumulating the datasets of optical products as observations in orbit proceed, and

related validation activities are ongoing. Although the retrieval of the aerosol optical properties can be realized stably, the

algorithms are still needed to be further optimized. The experience gained from analyzing the data acquired by ACDL has led

to many improvements, with significant room for optimization on low quality data and noise control. Various of further

algorithm improvement efforts are ongoing. Additionally, the ACDL scientific team is developing a unique scene classification

325 algorithm based on the aerosols and clouds optics products, which requires the improvement of the algorithms for optical

properties retrieval.

Data availability

ACDL-A data we used in this paper are not available publicly at the time when the article was submitted. We are allowed to

access the data through our participation as a part of ACDL scientific team. The ERA5 dataset are downloaded via the website

330 https://cds.climate.copernicus.eu/cdsapp#!/dataset/reanalysis-era5-pressure-levels?tab=form (last access: 11 July 2023).

Author contributions

G. Dai, S. Wu, J. Liu and W. Chen conceived of the idea for the retrieval of the aerosol and cloud optical properties; G. Dai

and W. Long wrote the manuscript; G. Dai, S. Wu, W. Long, K. Sun and F. Meng contributed to the algorithm development

and data analyses; J. Liu, Y. Xie, Z. Huang and W. Chen contributed to the scientific discussion. All the co-authors reviewed

335 and edited the manuscript.

Competing interests

The authors declare that they have no conflict of interest.

Acknowledgments

This study has been jointly supported by the Laoshan Laboratory Science and Technology Innovation Projects under grant

340 LSKJ202201202, the National Natural Science Foundation of China (NSFC) under grant U2106210, 61975191 and 41905022.

References

Balmes, K. A., Fu, Q., and Thorsen, T. J.: Differences in Ice Cloud Optical Depth From CALIPSO and Ground-Based Raman Lidar at the ARM SGP and TWP Sites. Journal of Geophysical Research: Atmospheres, 124, 1755-1778, https://doi.org/10.1029/2018JD028321, 2019.

345

Boucher, O., and Coauthors: Clouds and aerosols. Climate Change 2013: The Physical Science Basis, T. F. Stocker, Eds., Cambridge University Press, 571–657, 2013.

Bodhaine, B. A., Wood, N. B., Dutton, E. G., and Slusser, J. R.: On Rayleigh Optical Depth Calculations. Journal of Atmospheric and Oceanic Technology, 16, 1854-1861, 1999.

350 Burton, S. P., Ferrare, R. A., Hostetler, C. A., Hair, J. W., Rogers, R. R., Obland, M. D., Butler, C. F., Cook, A. L., Harper, D. B., and Froyd, K. D.: Aerosol classification using airborne High Spectral Resolution Lidar measurements – methodology and examples. Atmos. Meas. Tech., 5, 73-98, 2012.

Chen, W., Liu, J., Hou, X., Zang, H., Ma, X., Wan, Y., and Zhu, X.: Lidar Technology for Atmosphere Environment Monitoring Satellite, Aerospace Shanghai (in Chinese and English), 3, 13-20, 110, https://doi.org/10.19328/j.cnki.2096-

355 8655.2023.03.002, 2023.

Collis, R. T. H., and Russell, P. B.: Lidar measurement of particles and gases by elastic backscattering and differential absorption. Laser Monitoring of the Atmosphere, E. D. Hinkley, Ed., Springer Berlin Heidelberg, 71-151, 1976.

Dai, G., Sun, K., Wang, X., Wu, S., E, X., Liu, Q., and Liu, B.: Dust transport and advection measurement with spaceborne lidars ALADIN and CALIOP and model reanalysis data. Atmos. Chem. Phys., 22, 7975-7993, https://doi.org/10.5194/acp-22-

360 7975-2022, 2022.

Dong, J., Liu, J., Bi, D., Ma, X., Zhu, X., Zhu, X., and Chen, W.: Optimal iodine absorption line applied for spaceborne high spectral resolution lidar. Applied Optics, 57, 5413-5419, https://doi.org/10.1364/AO.57.005413, 2018.

Esselborn, M., Wirth, M., Fix, A., Tesche, M., and Ehret, G.: Airborne high spectral resolution lidar for measuring aerosol extinction and backscatter coefficients. Applied Optics, 47, 346-358, https://doi.org/10.1364/AO.47.000346, 2008.

365 Ehlers, F., Flament, T., Dabas, A., Trapon, D., Lacour, A., Baars, H., and Straume-Lindner, A. G.: Optimization of Aeolus' aerosol optical properties by maximum-likelihood estimation. Atmos. Meas. Tech., 15, 185-203, https://doi.org/10.5194/amt-15-185-2022, 2022.

Flamant, P., Cuesta, J., Denneulin, M., Dabas, A., and Huber, D.: ADM-Aeolus retrieval algorithms for aerosol and cloud products. Tellus A: Dynamic Meteorology and Oceanography, 2008.

370 Flament, T., Trapon, D., Lacour, A., Dabas, A., Ehlers, F., and Huber, D.: Aeolus L2A aerosol optical properties product: standard correct algorithm and Mie correct algorithm. Atmos. Meas. Tech., 14, 7851-7871, https://doi.org/10.5194/amt-14-7851-2021, 2021.

Garnier, A., Pelon, J., Vaughan, M. A., Winker, D. M., Trepte, C. R., and Dubuisson, P.: Lidar multiple scattering factors inferred from CALIPSO lidar and IIR retrievals of semi-transparent cirrus cloud optical depths over oceans. Atmos. Meas.

375 Tech., 8, 2759-2774, 2015.

Hunt, W. H., Winker, D. M., Vaughan, M. A., Powell, K. A., Lucker, P. L., and Weimer, C.: CALIPSO Lidar Description and Performance Assessment. J. Atmos. Oceanic Technol, 26, 1214-1228, https://doi.org/10.1175/2009JTECHA1223.1, 2009.

Hersbach, H., and Coauthors: The ERA 5 global reanalysis. Quart. J. Roy. Meteor. Soc., 146, 1999–2049, https://doi.org/10.1002/qj.3803, 2020.

380 Hu, Y.: Depolarization ratio–effective lidar ratio relation: Theoretical basis for space lidar cloud phase discrimination. Geophysical Research Letters, 34, 2007.

Illingworth, A. J., and Coauthors: The EarthCARE Satellite: The Next Step Forward in Global Measurements of Clouds, Aerosols, Precipitation, and Radiation. Bulletin of the American Meteorological Society, 96, 1311-1332 https://doi.org/10.1175/BAMS-D-12-00227.1, 2015.

385 IPCC: Climate Change 2013: The Physical Science Basis. Cambridge University Press, 1535 pp., https://doi.org/10.1017/CBO9781107415324, 2014.

IPCC: Annex I: Observational products. Climate Change 2021: The Physical Science Basis, V. Masson-Delmotte et al., Eds., Cambridge University Press, 2061–2085, 2021.

King, M. D., Kaufman, Y. J., Tanré, D., and Nakajima, T.: Remote Sensing of Tropospheric Aerosols from Space: Past, Present,

390 and Future, Bull. Amer. Meteorol. Soc., 80, 2229-2260, 10.1175/1520-0477(1999)080<2229:RSOTAF>2.0.CO;2, 1999.

Kar, J., Vaughan, M. A., Lee, K. P., Tackett, J. L., Avery, M. A., Garnier, A., Getzewich, B. J., Hunt, W. H., Josset, D., Liu, Z., Lucker, P. L., Magill, B., Omar, A. H., Pelon, J., Rogers, R. R., Toth, T. D., Trepte, C. R., Vernier, J. P., Winker, D. M., and Young, S. A.: CALIPSO lidar calibration at 532 nm: version 4 nighttime algorithm, Atmos. Meas. Tech., 11, 1459-1479, 10.5194/amt-11-1459-2018, 2018.

395 Ke, J., Sun, Y., Dong, C., Zhang, X., Wang, Z., Lyu, L., Zhu, W., Ansmann, A., Su, L., Bu, L., Xiao, D., Wang, S., Chen, S., Liu, J., Chen, W., and Liu, D.: Development of China's first space-borne aerosol-cloud high-spectral-resolution lidar: retrieval algorithm and airborne demonstration. PhotoniX, 3, 17, https://doi.org/10.1186/s43074-022-00063-3, 2022.

Li, Z., Liu Z., Yan Z., and Guo J.: Research on characters of the marine atmospheric boundary layer structure and aerosol profiles by high spectral resolution lidar. Optical Engineering, 47, 086001, https://doi.org/10.1117/1.2969122, 2008.

400 Liu, D., Zheng, Z., Chen, W., Wang, Z., Li, W., Ke, J., Zhang, Y., Chen, S., Cheng, C., and Wang, S.: Performance estimation of space-borne high-spectral-resolution lidar for cloud and aerosol optical properties at 532 nm. Optics Express, 27, A481-A494, https://doi.org/10.1364/OE.27.00A481, 2019.

Levy, R. C., Mattoo, S., Munchak, L. A., Remer, L. A., Sayer, A. M., Patadia, F., and Hsu, N. C.: The Collection 6 MODIS aerosol products over land and ocean. Atmos. Meas. Tech., 6, 2989-3034, https://doi.org/10.5194/amt-6-2989-2013, 2013.

405 Luthcke, S. B., Thomas, T. C., Pennington, T. A., Rebold, T. W., Nicholas, J. B., Rowlands, D. D., Gardner, A. S., and Bae, S.: ICESat-2 Pointing Calibration and Geolocation Performance, Earth Space Sci., 8, e2020EA001494, https://doi.org/10.1029/2020EA001494, 2021.

Legras, B., Duchamp, C., Sellitto, P., Podglajen, A., Carboni, E., Siddans, R., Grooß, J. U., Khaykin, S., and Ploeger, F.: The evolution and dynamics of the Hunga Tonga–Hunga Ha'apai sulfate aerosol plume in the stratosphere. Atmos. Chem. Phys., 410 22, 14957-14970, 2022.

Lohmar, F. J.: World geodetic system 1984 — geodetic reference system of GPS orbits, Berlin, Heidelberg, 1988, 476-486, 1988.

Müller, D., Hostetler, C. A., Ferrare, R. A., Burton, S. P., Chemyakin, E., Kolgotin, A., Hair, J. W., Cook, A. L., Harper, D. B., Rogers, R. R., Hare, R. W., Cleckner, C. S., Obland, M. D., Tomlinson, J., Berg, L. K., and Schmid, B.: Airborne 415 Multiwavelength High Spectral Resolution Lidar (HSRL-2) observations during TCAP 2012: vertical profiles of optical and microphysical properties of a smoke/urban haze plume over the northeastern coast of the US, Atmos. Meas. Tech., 7, 3487-3496, https://doi.org/10.5194/amt-7-3487-2014, 2014.

Pan, H., Huang, J., Kumar, K. R., An, L., and Zhang, J.: The CALIPSO retrieved spatiotemporal and vertical distributions of AOD and extinction coefficient for different aerosol types during 2007–2019: A recent perspective over global and regional 420 scales. Atmospheric Environment, 274, 118986, https://doi.org/10.1016/j.atmosenv.2022.118986, 2022.

Sayer, A. M., Smirnov, A., Hsu, N. C., and Holben, B. N.: A pure marine aerosol model, for use in remote sensing applications. Journal of Geophysical Research: Atmospheres, 117, https://doi.org/10.1029/2011JD016689, 2012.

Schuster, G. L., Vaughan, M., MacDonnell, D., Su, W., Winker, D., Dubovik, O., Lapyonok, T., and Trepte, C.: Comparison of CALIPSO aerosol optical depth retrievals to AERONET measurements, and a climatology for the lidar ratio of dust. Atmos. 425 Chem. Phys., 12, 7431-7452, https://doi.org/10.5194/acp-12-7431-2012, 2012.

Tenti, G., Boley, C. D., and Desai, R. C.: On the Kinetic Model Description of Rayleigh–Brillouin Scattering from Molecular Gases. Canadian Journal of Physics, 52, 285-290. https://doi.org/10.1139/p74-041, 1974.

Vaughan, M., Garnier, A., Josset, D., Avery, M., Lee, K. P., Liu, Z., Hunt, W., Pelon, J., Hu, Y., Burton, S., Hair, J., Tackett, J. L., Getzewich, B., Kar, J., and Rodier, S.: CALIPSO lidar calibration at 1064 nm: version 4 algorithm. Atmos. Meas. Tech., 430 12, 51-82, https://doi.org/10.5194/amt-12-51-2019, 2019.

Winker, D. M., Hunt, W. H., and McGill, M. J.: Initial performance assessment of CALIOP. Geophysical Research Letters, 34, https://doi.org/10.1029/2007GL030135, 2007.

Winker, D. M., Vaughan, M. A., Omar, A., Hu, Y., Powell, K. A., Liu, Z., Hunt, W. H., and Young, S. A.: Overview of the CALIPSO Mission and CALIOP Data Processing Algorithms. J. Atmos. Oceanic Technol, 26, 2310-2323, 435 https://doi.org/10.1175/2009JTECHA1281.1, 2009.

Wang, Q., Bu, L., Tian, L., Xu, J., Zhu, S., and Liu, J.: Validation of an airborne high spectral resolution Lidar and its measurement for aerosol optical properties over Qinhuangdao, China. Optics Express, 28, 24471-24488, https://doi.org/10.1364/OE.397582, 2020.

Young, S. A., and Vaughan, M. A.: The Retrieval of Profiles of Particulate Extinction from Cloud-Aerosol Lidar Infrared

440 Pathfinder Satellite Observations (CALIPSO) Data: Algorithm Description. Journal of Atmospheric and Oceanic Technology, 26, 1105-1119, 2009.

Young, S. A., Vaughan, M. A., Garnier, A., Tackett, J. L., Lambeth, J. D., and Powell, K. A.: Extinction and optical depth retrievals for CALIPSO's Version 4 data release. Atmos. Meas. Tech., 11, 5701-5727, 2018.

Yu, X., Chen, B., Min, M., Zhang, X., Yao, L., Zhao, Y., Wang, L., Wang, F., and Deng, X.: Simulating return signals of a

445 spaceborne high-spectral resolution lidar channel at 532 nm. Optics Communications, 417, 89-96, https://doi.org/10.1016/j.optcom.2018.02.046, 2018.

Zhang, Y., Liu, D., Zheng, Z., Liu, Z., Hu, D., Qi, B., Liu, C., Bi, L., Zhang, K., Wen, C., Jiang, L., Liu, Y., Ke, J., and Zang, Z.: Effects of auxiliary atmospheric state parameters on the aerosol optical properties retrieval errors of high-spectral-resolution lidar. Applied Optics, 57, 2627-2637, https://doi.org/10.1364/AO.57.002627, 2018.